Morphology and microstructure of chromite crystals in chromitites from the Merensky Reef (Bushveld Complex, South Africa)

Zoja Vukmanovic • Stephen J. Barnes • Steven M. Reddy • Bélinda Godel • Marco L. Fiorentini

Zoja Vukmanovic

The University of Western Australia, Centre for Exploration Targeting, ARC Centre of Excellence for Core to Crust Fluid Systems, Crawley, WA 6009, Western Australia
CSIRO Earth Science and Resource Engineering, Australian Research Center, Kensington, WA 6151, Australia

Stephen J. Barnes

CSIRO Earth Science and Resource Engineering, Australian Research Center, Kensington, WA 6151, Australia

Steven M. Reddy

Curtin University, Department of Applied Geology, PO Box U1987, Perth WA 6845, Australia

Bélinda Godel

CSIRO Earth Science and Resource Engineering, Australian Research Center, Kensington, WA 6151, Australia

Marco L. Fiorentini

Centre for Exploration Targeting , The University of Western Australia , ARC Centre of Excellence for Core to Crust Fluid Systems, Crawley, WA 6009, Western Australia

Abstract

The Merensky Reef of the Bushveld Complex consists of a lower chromitite layer, a coarse-grained melanorite and upper chromitite layer. Detailed microstructural analysis of chromitite layers using electron backscatter diffraction analysis (EBSD), high-resolution X-ray microtomography and crystal size distribution analyses distinguished two populations of chromite crystals: fine grained idiomorphic and large silicate inclusion bearing crystals. The lower chromitite layer contains both populations, whereas the upper contains only fine idiomorphic grains.

Electron backscatter diffraction data shows absence of crystallographic preferred orientation and shape preferred orientation in both layers. Most of the inclusion-bearing chromites have characteristic amoeboidal shapes that have been previously explained as product of sintering of pre-exisiting smaller idiomorphic crystals. Here, two possible scenarios are proposed to explain the sintering process in chromite crystals: 1) amalgamation of a cluster of grains with the same original crystallographic orientation; and 2) sintering of randomly orientated crystals followed by annealing. The EBSD data show no evidence for earlier presence of idiomorphic subgrains spatially related to inclusions, nor for clusters of similarly oriented grains among the idiomorphic population, and therefore argue against a sintering model. An alternative is proposed whereby silicate inclusions are incorporated during maturation and recrystallisation of initially dendritic chromite crystals.

Electron backscatter diffraction analysis maps show deformation-related misorientations and curved subgrain boundaries within the large, amoeboidal crystals, and absence of such features in the fine grained population. The deformation record is highly dependent on the size and the shape of the crystals. Microstructures observed in the lower chromitite layer are interpreted as the result of deformation during compaction of the orthocumulate layers, and

constitute evidence for the formation of the amoeboid morphologies at an early stage during consolidation.

Keywords: Merensky Reef; chromite; microstructures; Electron backscatter diffraction (EBSD)

Introduction

The Merensky Reef of the Bushveld Complex (Fig. 1) is one of the most studied bodies of igneous rock in the world, and yet still one of the most enigmatic. (Naldrett, et al. 2009a; Naldrett, et al. 2011b). Among the less understood features of this predominantly melanoritic layer is the presence of very thin but extraordinarily extensive chromitite layers that carry a high proportion of the platinum group elements (PGEs) in the Reef. Understanding these chromitite layers is the key to understanding the PGE concentrations, and to unravelling the petrogenesis of the Reef as a whole.

The Merensky Reef for most of its strike length overlies an anorthosite and it comprises a lower chromitite layer (0.7-1 cm in thickness), a coarse-grained melanorite (CGM; ~10 cm in thickness), an upper chromitite (~1 cm in thickness) and an overlying melanorite (Fig 1c); (Ballhaus and Sylvester 2000; Barnes and Maier 2002; Cawthorn and Boerst 2006; Eales and Reynolds 1986; Elhaddad 1996; Maier and Bowen 1996; Naldrett, et al. 1986; Naldrett, et al. 2009b; Nicholson and Mathez 1991). This study is a detailed comparative study of the lower and upper chromitite layers.

The Lower Chromitite layer contains a population of unusual “amoeboid” chromite grains characterised by re-entrant morphologies and abundant poly-mineralic silicate inclusions. Silicate inclusions in chromite crystals are very common in geological settings such as layered intrusions (Irvine 1975; Spandler, et al. 2005) and ophiolite complexes (Greenbaum 1977; Peters and Kramers 1974; Talkington, et al. 1983) and the origin of such inclusions has been debated for more than 50 years (Ballhaus and Stumpfl 1986; Barnes and Maier 2002;

Cameron 1978; Hulbert and Von Gruenewaldt 1985; Li, et al. 2005; McDonald 1965). In the Merensky Reef, the inclusions consist mainly of polymineralic aggregates of Na-phlogopite and orthopyroxene, with minor hornblende, K-phlogopite, oligoclase and quartz (Ballhaus and Stumpfl 1986; Li, et al. 2005; Spandler, et al. 2005) and have been attributed to the involvement of a fluid phase during solidification of the Merensky Reef (Ballhaus and Stumpfl 1986; Li, et al. 2005; Mathez, et al. 1994). Alternatively, the mechanism of inclusion entrapment of these inclusions has been attributed to amalgamation (referred to as sintering) of multiple fine grained idiomorphic chromite crystals into larger single chromite crystals with incorporation of highly differentiated trapped intercumulus liquid (Hulbert and Von Gruenewaldt 1985).

The aim of this study is to expand the knowledge of chromite textures, crystallographic orientation, grain morphology, composition and internal microstructures within the Merensky Reef chromitites. New microstructural data (by electron backscatter diffraction analysis) are combined with 2D and 3D quantitative petrography (crystal size distribution and high resolution X-ray computed tomography) and microprobe data on chromite crystals. Results are synthesized to address the problem of how two compositionally similar layers ten to twenty centimeter apart, within a thick body of slowly cooled cumulates, came to have striking textural differences; specifically, why silicate melt inclusions are abundant in the lower layer but absent in the upper. Our findings have broader implications for the petrogenesis of the Reef as a whole.

Methodologies

2D and 3D Image analysis

Chromite crystals were manually segmented and separated from reflected-light photomicrograph mosaics of whole thin sections to create binary images, which were

processed using ImageJ 1.43u software to measure length, width, area, and equivalent circle diameter (ECD) for each crystal. Crystal solidity (see electronic appendix) was calculated separately in MatLab. Crystal-size distribution of chromites were calculated using an updated version of CSDToolBox software (Ricard, et al. 2012). Methodology for the high resolution X-ray computed tomography is given by Godel et al (2010).

Electron Backscatter Diffraction Analysis (EBSD)

Electron backscatter diffraction data were collected by using a Zeiss Evo 40XVP SEM at Curtin University of Technology (Perth, Western Australia). All EBSD data have been processed using Oxford Instruments software package CHANNEL 5 software (for more details see electronic appendix and supplementary table 1). The typical precision for EBSD lattice orientation analysis on this instrument is less than 0.5°. Samples were prepared according to usual EBSD protocols (Prior, et al. 1999; Reddy, et al. 2007). Two samples that contain accessory sulphide phases were further polished using a broad ion beam polisher, resulting in pronounced ridges at the edges of the chromite grains causing apparent changes in the crystal lattice of up to 2° (later referred to as a edge effect).

Data were processed to create inverse pole figure and pole figure maps showing the crystallographic orientation of the analysed grains, and texture component maps showing relative differences in within-grain lattice orientation (Wheeler, et al. 2003). Grain size maps, where grains are colour coded by size, were used to evaluate grain-size dependent crystallographic preferred orientation (CPO). Crystallographic orientation data were plotted on stereograms using lower-hemisphere equal-area projections. Analyses of misorientation angle data relative to theoretical distributions of random cubic grains were undertaken to assess the extent of any crystallographic preferred orientation within the samples. The minimum misorientation angle (Wheeler, et al. 2001) was calculated between 1000 randomly selected diffraction patterns.

Mineral chemistry analyses

Major element concentration analyses were performed at the Center for Microscopy, Characterisation and Analysis at the University of Western Australia (Perth, Western Australia), on a JEOL 85390F electron microprobe using 15kV accelerating voltage and 20nA beam current. We used a chromite standard for the chromium, aluminum and iron, nickel and vanadium metals for nickel and vanadium, rutile for titanium, periclase for magnesium, and manganotantalite for manganese. A Zeiss Ultraplus Field Emission SEM at the Australian Resources Research Centre (CSIRO, Kensington, Western Australia) was used for elemental mapping and imaging under operating conditions of 20kV accelerating voltage and 5nA beam current.

Petrography

The samples studied here are polished sections of "normal" Merensky Reef (normal reef referes to reef with two chromitite layers 15 to 30 cm apart (Naldrett, et al. 2009c)) from the Rustenburg Platinum Mine (western limb of the Bushveld Complex, Fig.1a, b). The same polished sections have been studied in detail by Godel et al. (2008; 2006; 2007; 2010)..

Lower chromitite layer

The contact between the lower chromitite layer and the underlying anorthosite is irregular at the centimeter scale (Godel and Barnes 2008; Godel, et al. 2006); (Fig. 2a). The anorthosite is composed mostly of plagioclase with minor poikilitic orthopyroxene and trace sulphide minerals (Godel, et al. 2006). Plagioclase (up to 2 mm) shows a layer-parallel lamination and characteristic wedge-shaped (deformation) twins.

The lower chromitite is around 1cm thick and contains two morphologically distinct groups of chromite grains (Fig. 2a). The larger chromite crystals (~ 2 mm) show "amoeboidal" morphologies and frequently contain spherical silicate inclusions (Fig. 2b) and tubular embayments. High-resolution X-ray computed tomography (Fig. 3a, b) reveals that most of

the inclusions are spherical and octahedral aggregates. However, tubular embayments extending to the grain margins are also present and may appear to be fully enclosed inclusions in two dimensional sections (Fig. 3a). The silicate inclusions commonly occur in 3D as clusters within individual amoeboidal grains (Fig. 3b). Scanning electron microscopy analysis indicates these inclusions are composed mainly of polymineralic aggregates of orthopyroxene, clinopyroxene, biotite, phlogopite, apatite and rutile. Individual crystals may contain more than fifty separate inclusions randomly distributed within the crystal (Fig. 3b). The second population of chromites shows idiomorphic octahedral shapes (Fig. 2a). These octahedral crystals are much finer (<500 μm) than the amoeboidal crystals and are entirely devoid of silicate inclusions. The dominant interstitial phases are plagioclase (39% by volume) and orthopyroxene (10%). Base-metal sulphides consisting of intergrowth of pyrrhotite ($Fe_{1-x}S$), pentlandite ($(Fe, Ni)_9S_8$ and chalcopyrite $FeCuS_2$) are present as minor components (1 %). The sulphides occur either as an interstitial phase between chromite and silicate grains or more rarely as inclusions within chromites or silicates.

Upper chromitite layer

The upper chromitite layer has irregular planar upper and lower boundaries (Godel and Barnes 2008; 2006). The layer comprises ~55% by volume chromite, ~23% orthopyroxene, ~22% plagioclase and ~1% of sulphide phases. The finer-grained chromite crystals (from 100μm up to 400μm) are almost exclusively idiomorphic (Fig. 2 d, e; Fig. 3c) and do not contain silicate or sulphide inclusions (Fig. 2e). They are mostly “immersed” in plagioclase, with limited number of chromite crystals occurring along the orthopyroxene grain boundaries (Godel et al 2006). As in the coarse grained melanorite that separates the two chromitite layers, plagioclase shows deformation twins (Fig. 2f).

Results

Crystal size distribution of chromite

Crystal size distribution analysis was introduced to the study of igneous rocks by Marsh and others and provides information on growth rate and nucleation mechanisms (Higgins 2000; Marsh 1988). A total of 746 crystals and 2953 crystals were measured within the lower and upper chromitite layers, respectively (Fig. 4a, c). The crystal-size distribution curve of chromite from the lower chromitite layer is concave (Fig 4b) for the fine grain chromite crystals (up to 500 μm ECD) and then flattens to become linear for larger chromite crystal size. In contrast, the CSD curve from the upper chromitite is slightly concave (Fig 4d), reflecting a deficiency of crystals in the range 50 to 100 μm ECD. The crystal size distribution curve is almost perfectly linear with relatively steep slope (Fig. 4d) at larger crystal sizes.

Orientation Analysis

Orientations of chromite grains in the two layers were investigated using EBSD to enable testing of alternative models for formation of inclusion-rich and amoeboid crystals. EBSD is the only technique that allows this kind of information to be determined on cubic minerals.

Lower chromitite

The inverse pole figure (IPF) orientation map of chromite grains from the lower chromitite indicates no consistent grain orientation (Fig. 5a). This is confirmed by the inverse pole figures that show crystal orientations with respect to the specimen XYZ coordinate framework (Fig. 5c) and the distribution of misorientation angles relative to the theoretical distribution of random cubic grains (Fig 5d). A small peak at <5° misorientation angle indicates a slight increase in low-angle misorientation angles above random (see below).

However, the orientation data from the lower chromitite indicate that chromite grains have a random orientation.

The grain size map (Fig. 5b) confirms the grain size distribution and shape types identified petrographically (Fig. 2). Inverse pole figures, coloured for grain size (Fig. 5d), indicate that there is no relationship between grain size and grain orientation. Similar maps looking at grain shape, e.g. the long axes of ellipses fitted to the grains (not reproduced here), also fail to show any correlation between shape and crystallographic-preferred orientation. There is no evidence of local clustering of orientations, i.e. adjacent or touching grains having the same orientations.

Upper chromitite

Chromite grains from the upper chromitite show a range of orientations (Fig. 6a), with no consistent orientation in the IPF plot (Fig. 6c). Misorientation angles show a perfect match to the theoretical random distribution (Fig. 6d). In contrast to the data from the lower chromitite sample, there is no peak above the theoretical random distribution fit in the low-angle misorientation angle data. The chromites in the upper chromitite show an entirely random distribution of grain orientations.

Intragrain microstructure of chromite grains

Lower chromitite

Within the lower chromitite, the large allotriomorphic, "amoeboidal" chromites, which are embayed and contain abundant inclusions, show significant intragrain lattice variations (Fig. 7a). Electron backscatter diffraction data shows that amoeboidal chromites are single crystals with intragrain distortions ranging up to 12° of misorientation (Fig. 7a, b). These variations are seen as both gradual, progressive changes across significant areas of the grain and as discrete low-angle boundaries. Low-angle boundaries (<10°) are commonly localized in the areas of grains between embayments and inclusions (Fig. 7a). Most of the low angle subgrain

boundaries (up to 5°) are curved whereas straight subgrain boundaries are less common and usually are at slightly higher angles (>7°). A small peak at around 5° in the misorientation angle distribution histogram corresponds to these low angle subgrain boundaries (Fig. 5d, 7a). In contrast, the smaller idiomorphic chromite grains show little internal lattice variations and no development of subgrain boundaries (Fig. 7c). Small misorientations (<2°) localized at grain edges show no systematic orientation characteristics and are likely to be due to edge effects and polishing artifacts.

Grain 6 on Figure 7a belongs to the class of larger grains, exceeding 500μm in size but with relatively idiomorphic shape. This grain shows very mild misorientation of only 1-2° disorientated relative to its neighboring pixel.

Upper chromitite

The small octahedral grains in the upper chromitite show maximum internal misorientation of 2° (Fig. 8a). Regions of slightly stronger internal misorientation (Fig. 8a, grains 1 to 2) are artifacts caused by the broad ion beam polishing. Grains 3 and 4 have been polished only with colloidal silica and do not show ridge effects. Despite the edge effect, chromites from upper chromitite layer do not show evidence for intragrain lattice distortion and no significant subgrain structure is apparent in this population of grains (Fig. 8a).

Chromite in the upper chromitite layer often form clusters of crystals or a crystal chains (Fig. 8b). Analyses of crystal aggregate in one such structure (Fig 8b) indicate that the “host” (light green) grain is differently oriented respect to each of the adjacent grains (Fig 8b) and there is no systematic orientation relationship between the host grain and its surrounding neighbors (Fig 8c).

Chromite compositions

In the lower chromitite layer, both idiomorphic and amoeboidal chromites show relatively homogenous compositions and little detectable chemical zonation from cores to rims of the

crystal (Table 1; Fig. 9). Unlike results from Li et al. (2005) our data show no systematic distinction between inclusion bearing chromites and inclusion free grains (Fig. 9). Chromites from the lower chromitite layer have relatively wide ranges of major element composition, showing no strong trend.

Chromite crystals from the upper chromitite layer show little or no chemical variation between cores and rims. Unlike chromites from the lower chromitite layer, $100Mg/(Mg+Fe^{2+})$ vs $100Cr/(Cr+Al)$ and Fe_2O_3 vs $100Cr/(Cr+Al)$ show strong positive an negative correlations respectively (Fig. 9).

Chromite crystals from the lower chromitite layer show significantly higher Mg number values compared with chromite crystals from the upper chromitite values (Table 1, Fig. 9). Opposite from Mg, lower chromitite crystals show lower values of Cr number, Ti and Fe than the crystals from the upper chromitite later.

Major and trace elemental mapping was carried out on one of the large amoeboidal grains from the lower chromitite. Chromium, Fe, Al, Ni, and V are homogenously distributed within the chromite crystals. In contrast, Ti concentrations within the crystals (Fig. 10) vary and correspond to fine TiO_2 (rutile) exsolution, present throughout the whole chromite crystal (Fig. 10d). Rutile exsolution lamellae are present in both core and rim of both idiomorphic and amoeboidal chromite crystals.

Chromite crystals from the upper chromitite layer have relatively homogenous major and trace element concentration (Fig. 11c). Fewer TiO_2 exsolution lamellae are observed within these grains (Fig. 11c). They have very fine needle like shape and occur either at chromite crystal boundaries (Fig. 11c) or dispersed throughout host grains (Fig. 11d).

Quantification of morphology and accumulated mean deformation in the chromite crystals

Chromite crystal morphology is defined by its size and its solidity (area divided by convex hull area using a Matlab code). Solidity of 1 indicates the crystal has a convex (circular) shape whereas decreasing further away from 1, the shape shows more concave borders. Amoeboidal grains have lower solidity values (<0.9) whereas idiomorphic grains have solidity closer to 1. Crystal morphology is compared to the amount of deformation within individual crystals, as measured by the average misorientation, determined from the EBSD data. High average misorientations imply high degrees of internal deformation.

Apart from the data cluster with high solidity values (0.8-1), the mean misorientation data and the size data show a weak positive trend with most of the crystals with lower values of solidity (i.e. the more irregularly shaped grains) showing larger mean misorientation (Fig. 12). Deviation from the linear relationship can be due to a stereological effect and is largely due to the fact that not all large crystals are deformed. Solidity (size and colour of the symbols on the Fig. 12) can be used to discriminate between amoeboidal and octahedral grains (Fig. 12a).

In the case of the upper chromitite layer, the mean misorientation – size – solidity graph (Fig. 12b) shows no clear trend. The majority of the grains record less than 1° of mean misorientation and are significantly smaller, more regular and less deformed than the chromites from the lower chromitite layer. Only the few grains that show low values for solidity (<0.7) have very low mean misorientation values. In the upper as well as in the lower chromitite layers, two grains are showing unexpected results with high mean misorientation and small size and solidity.

Both lower and upper chromitite layers have overlapping populations (the gray cloud on the Fig. 12a) of small undeformed chromite crystals. These similar grains are very small in size ($<0.3\mu m^2$) and have mean misorientation values smaller than 1.2°.

Discussion

Genetic models for the Merensky Reef need to explain some significant differences in the morphology, microstructure and chemistry of chromite between the upper and lower chromitite layers, as documented in this study.

(**1**) The two chromite layers have markedly different populations in terms of crystal size and shape. The lower chromitite layer has a population of large, inclusion-bearing amoeboidal grains absent from the upper layer. This contributes to a complex crystal size distribution in the lower layer, with multiple changes in slope of the CSD curve. In contrast, the CSD curve of the chromites in the upper chromitite layer is almost perfectly linear and with very steep slope, indicating steady state crystallisation (Marsh 1988).

(**2**) Polymineralic hydrous silicate inclusions are almost entirely restricted to the amoeboid grains, which are also characterized by tubular re-entrant features in their 3D morphologies.

(3) No evidence of crystallographic preferred orientation and shape preferred orientation is seen in either chromitite layers. Chromite crystals that are part of crystal aggregates show different crystallographic orientation than their direct neighbors (Fig. 8).

(**4**) EBSD mapping shows that substantial internal deformation is restricted to the large amoeboidal grains (Fig 7, 11). Such microstructures are formed by a dislocation creep mechanism (Passchier and Trouw 2005), which is characteristic of temperatures above 1000°C on the basis of experimental data (Cordier 2002; Karato, et al. 1998). This observation indicates that the amoeboidal grains attained their present morphologies before or during deformation of the crystal pile. Idiomorphic crystals from both upper and lower chromitite exhibit no significant intra-grain orientation variations, (Fig. 8, 11).

(**5**) Chromite in the lower and upper layers have contrasting major element compositions, the lower chromitite showing lower 100Cr/(Cr+Al), higher magnesium number (Mg#) and lower TiO_2 and Fe_2O_3 (Table 1, Fig. 9).

The differences between the two layers have to be interpreted in the context of the two chromite layers occurring a few tens of cm apart, within a thickness of several km of slowly-cooled cumulates. Their post-cumulus cooling histories are likely to have been identical. These observations place useful constraints on the relative timing of crystallisation, grain size modification, inclusion entrapment and deformation of the crystal pile.

Implications for the magmatic evolution of Merensky Reef

A variety of explanations has been proposed for inclusion entrapment in chromite crystals (Ballhaus and Stumpfl 1986; Barnes and Maier 2002; Cameron 1978; Hulbert and Von Gruenewaldt 1985; Li, et al. 2005; McDonald 1965). We here consider two alternative hypotheses, and evaluate them in the light of the data presented in this study: firstly a "sintering" model involving amalgamation of multiple grains; and secondly, a model involving textural evolution of originally dendritic crystals. The widely accepted model of Hulbert and Von Gruenewaldt (1985) suggests that amalgamation of different grains occurred along the triple junctions due to the high local stresses in presence of reactive liquid. During this process, silicate melt is entrapped at the original contact points. The end result could be either an aggregate of grains in different orientation having the external appearance of a single crystal (Fig. 13a), or an actual single crystal (Fig. 13b). The EBSD data on the amoeboid grains clearly rule out the former option (Fig. 7), but the latter option requires consideration in the light of the EBSD data set as a whole.

There are two possible mechanisms by which single crystals could form from sintering of multiple grains. The first requires amalgamation of a cluster of grains with the same original orientation, possibly developed in the first place as a result of epitaxial self nucleation (i.e.

nucleation of new crystals on older ones in the same orientation). This mechanism is counter to the evidence from the EBSD data (Fig. 5, 7). Random orientation of the small idiomorphic population in both layers and the absence of systematic misorientation axes in the chromite aggregates from the upper chromitite layer indicate that epitaxial self-nucleation did not occur in either of the two chromitite layers (Fig 5, 6, 7, 8).

If the "sintered" grains were not originally in the same orientation, an annealing process needs to be considered, whereby differently oriented crystals recrystallised into a single grain (Fig. 13b). Annealing, also referred to as grain boundary migration recrystallisation, is one of the processes characteristic of recovery of the crystal structure (Passchier and Trouw 2005). At relatively high temperature, grain boundary mobility increases to an extent that grain boundaries can sweep through the entire crystal and remove the dislocations and subgrain boundaries in the crystal (Passchier and Trouw 2005). In the model proposed by Hulbert and Von Gruenewaldt (1985) the recrystallisation process would have to follow the sintering, to account for the observation that inclusion-bearing chromites are single crystals.

The mechanism of complete post-sintering recrystallisation seems to be implausible, for the following reasons. Recrystallisation would be unlikely to completely remove all traces of the original internal grain boundaries. Subgrain boundaries, imaged by EBSD mapping (Fig. 7), would be expected to show spatial relationship to the location of the silicate inclusions that mark the original pre-sintering grain boundary. This is not observed in the EBSD maps, which show that subgrain boundaries are deformation features related to external morphology, not to inclusions. Furthermore, the distance between two chromitite layers is only 10-20 cm, and hence the two layers must have experienced essentially identical sub-liquidus cooling histories. Amoeboid grains are restricted to the lower chromite layer while the population of small equant inclusion-free crystals is common to both layers. A sintering

model fails to account for a restriction of inclusion-bearing grains to the lower chromitite layer only.

The sintering mechanism as proposed by Hulbert and Von Gruenewaldt (1985) is driven essentially by interaction between chromite crystals and trapped intercumulus melt. Such interaction produces a very distinctive trend in chromite compositions, whereby Ti and Fe^{3+} increase as these components become enriched in the liquid, Mg/Fe decreases due to exchange with coexisting ferromagnesian silicates and Cr/Al increases in response to changing activity-composition relations in the spinel solid solution (Roeder and Campbell 1985). This trend, commonly termed the "Rum Trend" (Barnes and Roeder 2001; Henderson and Wood 1981) is a characteristic feature of Critical Zone chromites (Naldrett, et al. 2011a), and is seen in the trend from the lower to the upper chromite layer in this study (Table 1, Fig. 9). The upper chromite layer has evidently undergone more extensive reaction with trapped liquid than the lower layer, the opposite of what would be expected if the amoeboid chromites of the lower layer are the result of trapped liquid interactions. This constitutes further evidence against a sintering model.

In the absence of evidence for sintering, we interpret the EBSD, CSD, microprobe and grain shape data to indicate that the amoeboid inclusion-bearing chromites grew initially as single crystals at the liquidus. Critical to this interpretation is the observation that the amoeboid chromites have a distinctive combination of features: complex, embayed and convex morphologies; abundant inclusions, and internal deformation features that indicate the grains had attained their current complex morphologies while the crystal pile was still compacting. We interpret the grain morphologies in terms of two-stage growth involving an initial dendritic growth stage (Fig. 13c). This hypothesis follows (Leblanc 1980), who suggested that nodular chromites from Troodos ophiolite have been remodified from skeletal to nodular

habit, and that silicate inclusions within chromite grains are a consequence of this mechanism.

Dendritic chromites are found in komatiites (Arndt, et al. 1977; Barnes 1985; Dowling, et al. 2004; Godel, et al. 2012; Shore and Fowler 1999; Zhou and Kerrich 1992) and ophiolite complexes (Greenbaum 1977; Leblanc 1980) and contain polymineralic silicate assemblages in between the dendritic branches. Dendrites have been interpreted as a product of rapid cooling (Chalmers 1964); however, they are often found in plutonic rocks where cooling rates should have been slow (Donaldson 1982). In such cases, dendritic morphologies are the result of rapid rates of crystal growth relative to diffusion supply of nutrients, and are the consequence of sudden events that induce constitutional supercooling, such as pressure changes due to rapid volatile exsolution or eruption of magma from a chamber, catastrophic mixing events, or influx of hot magma against a cooler crystal pile.

We follow Cawthorn and Boerst (2006), Naldrett, et al. (2011b) and many other workers in interpreting the base of the Merensky unit, on a wide range of geological, isotopic and mineral chemistry evidence, as the influx of hot new magma at a major magmatic unconformity, across a floor of cooler and partially molten anorthosite. Such model is in agreement with the major element geochemistry presented in this study. Chromite saturation of Merensky reef magmas can be caused by mixing with resident magma or by contamination with partial melts derived from the underlying anorthosite (Ballhaus 1998; Ballhaus and Ryan 1995; Irvine 1975; Irvine 1977). Saturation in chromite gave rise to a population of small euhedral grains (represented by the linear CSD) with a small number of dendritic grains arising from rapid cooling against the anorthosite. Periods of rapid growth from a small number of nucleii resulting in dendritic crystal growth are supported by kinked CSD curve for the lower chromitite layer. During subsequent crystallisation, these dendrites experienced modification of their morphology in an attempt to attain lower surface areas and greater

textural equilibrium. This process gave rise to smooth grain boundaries, and necking off of original concavities to form inclusions of silicate melt. The textural maturation process took place over a range of temperatures but culminated close to the solidus, allowing chromite to incorporate pockets of highly differentiated, trapped intercumulus melt, accounting for the unusually evolved compositions of the inclusions (Ballhaus and Stumpfl 1986; Li, et al. 2005).

The origin of the two chromite layers from the Merensky Reef has been interpreted as a result of two different impulses of magma (Cawthorn and Boerst 2006). The addition of the second pulse of magma, from which the upper chromitite layer crystallized, caused coarsening of the orthopyroxene in the coarse grained melanorite and triggered textural re-equilibration of the lower chromite (Fig. 14b, b_1), giving rise to the kinked crystal size distribution curve for the lower chromitite grains. Electron microprobe data that shows similar chemistry for the two populations of lower chromitite grains implies a two stage crystallisation event rather than a process of mechanical mixing of the two chromite populations (Fig. 4b). During prolonged cooling of the crystal pile following the magma influx event, modification of initially dendritic chromites occurred through a ripening process whereby those parts of the grains with the highest surface area dissolved while the more energetically stable surfaces grew (Fig $14b_1$).

Previous microstructural work on silicates from Merensky Reef at Impala (Barnes and Maier 2002) and Rustenburg (Godel, et al. 2006) and textural analysis on silicates from the transitional zone between Lower and Critical zone (Boorman, et al. 2004), have been both interpreted as compaction-related textures, accompanying buoyancy-driven expulsion of intercumulus melt. At this stage, the amoeboidal chromites started to accommodate strain through crystal plasticity (Fig. 14c). Deformation was recorded selectively depending on the size and shape of the crystals (Fig, 12; Fig. $14c_1$ and c_2). Larger irregular grains

accommodated the strain by forming subgrain boundaries, while the small equant grains record minimal or no internal deformation. Crucially, the relationship of deformation microstructures to grain morphology is evidence that the amoeboidal chromites attained their irregular morphologies early in the solidification process, and not in the latest stages of solidification as required by sintering mechanisms. However, the highly evolved nature of the polymineralic silicate inclusions requires final entrapment close to the solidus. The evolution of the amoeboidal chromite grains therefore spans the temperature range from liquidus to solidus, consistent with our model for textural modification of original dendrites.

Conclusions

1) Chromites in the lower chromite layer consist of two populations, one of equant regular grains showing linear homogenous crystal size distributions, and a second population of large “amoeboid” grains with highly embayed re-entrant morphologies and abundant composite silicate inclusions. The upper chromitite layer contains only the equant population and has somewhat more primitive chromite compositions;

2) Electron backscatter diffraction analysis demonstrated that the amoeboid chromite crystals from the lower chromitite layer were single crystals and not amalgamations of several crystals. These chromites, but not the equant grain population, contain high temperature internal microstructures. Subgrain boundaries are interpreted as early magmatic deformation microstructures, and are most likely due to the compaction and cooling of the magmatic column above the solidus temperature.

3) The relationship of deformation microstructures to chromite grain morphology is evidence that the amoeboidal chromites attained their irregular morphologies at the cumulus stage, but the evolved nature of the silicate inclusions requires entrapment close to the solidus. The amoeboidal chromite textures developed over the temperature range from liquidus to solidus.

4) Based on microstructural observations, chemical compositions and crystal size distribution curves, the origin of the inclusion bearing chromites is unlikely to be due to amalgamation and sintering of originally separate multiple grains. It is more likely to be related to the modification of primary dendritic chromite morphologies, formed by rapid initial crystallisation in a thermal boundary layer between hot incoming magma and a cooler eroded crystal pile beneath, followed by textural maturation during solidification and compaction. The upper chromite layer was emplaced on a hotter substrate with no supercooling, and hence no dendrites. This accounts for the differences between the upper and lower chromite.

Acknowledgment

This work was funded by the Commonwealth Scientific and Industrial Research Organisation (CSIRO) Flagship Scholarship, The University of Western Australia Scholarship for International Research Fees and a Top-up scholarship from Minerals and Energy Research Institute of Western Australia to Zoja Vukmanovic. David Adams (CMCA, UWA) and Michael Verral (CSIRO) are acknowledged for assistance during spot analyses with electron microprobe and elemental map acquisition with scanning electron microscopy. We thank Dr Christoph Schrank for his constructive comments, long discussions during the early stage of the paper and for his help with MatLab code implementation. We also want to thank Dr Mark Jessell and Dr Angela Halfpenny for the constructive discussion. This paper is a contribution from the CSIRO Minerals Down Under National Research Flagship.

Reference

Arndt NT, Naldrett AJ, Pyke DR (1977) Komatiitic and iron-rich tholeiitic lavas of Munro Township, northeast Ontario. Journal of Petrology 18:319-369

Ballhaus C (1998) Origin of podiform chromite deposits by magma mingling. Earth and Planetary Science Letters 156(3-4):185-193 doi:10.1016/s0012-821x(98)00005-3

Ballhaus C, Ryan CG (1995) Platinum-group elements in the Merensky reef. I. PGE in solid solution in base metal sulfides and the down-temperature equilibration history of Merensky

ores. Contributions to Mineralogy and Petrology 122(3):241-251 doi:10.1007/s004100050124
Ballhaus C, Stumpfl EF (1986) Sulfide and platinum mineralization in the Merensky Reef: evidence from hydrous silicates and fluid inclusions. Contributions to Mineralogy and Petrology 94:193-204.
Ballhaus C, Sylvester P (2000) Noble metal enrichment processes in the Merensky Reef, Bushveld Complex. Journal of Petrology 41:545- 561
Barnes S-J (1985) The petrography and geochemistry of komatiite flows from the Abitibi greenstone belt, and a model for their formation. Lithos 18:241-270.
Barnes S-J, Maier WD (2002) Platinum-group Elements and Microstructures of Normal Merensky Reef from Impala Platinum Mines, Bushveld Complex. Journal of Petrology 43(1):103-128 doi:10.1093/petrology/43.1.103
Barnes SJ, Roeder PL (2001) The range of spinel compositions in terrestrial mafic and ultramafic rocks. Journal of Petrology 42:2279- 2302
Boorman S, Boudreau A, Kruger FJ (2004) The Lower Zone-Critical Zone Transition of the Bushveld Complex: a Quantitative Textural Study. Journal of Petrology 45(6):1209-1235
Cameron EN (1978) The lower zone of the eastern Bushveld Complex in the Oliphants River Trough. Journal of Petrology 19:437-462
Cawthorn RG, Boerst K (2006) Origin of the Pegmatitic Pyroxenite in the Merensky Unit, Bushveld Complex, South Africa. J Petrol 47(8):1509-1530
Chalmers B (1964) Principles of solidification. New York : John Wiley
Cordier P (2002) Dislocations and Slip Systems of Mantle Minerals. Reviews in Mineralogy and Geochemistry 51(1):137-179 doi:10.2138/gsrmg.51.1.137
Donaldson CH (1982) Origin of some Rhum harrisite by segregation of intercumulus liquid. Mineralogical Magazine 45:201-209
Dowling SE, Barnes SJ, Hill RET, Hicks JD (2004) Komatiites and nickel sulfide ores of the Black Swan area, Yilgarn Craton, Western Australia. 2: Geology and genesis of the orebodies. Mineralium Deposita 39(7):707-728
Eales HV, Reynolds IM (1986) Cryptic variations within chromitites of the Upper Critical Zone, Northwestern Bushveld Complex. Economic Geology 81:1056-1066
Elhaddad MA (1996) The first occurrence of platinum group minerals (PGM) in a chromite deposit in the Eastern Desert, Egypt. Mineralium Deposita 31(5):439-445
Godel B, Barnes S-J (2008) Image analysis and composition of platinum-group minerals in the J-M Reef, Stillwater Complex. Economic geology and the Bulletin Of the Society Of Economic Geologists 103(3):637-651
Godel B, Barnes S-J, Maier WD (2006) 3-D distribution of sulphide minerals in the Merensky Reef (Bushveld Complex, South Africa) and the J-M Reef (Stillwater Complex, USA) and their relationship to microstructures using X-ray computed tomography. Journal of Petrology 47:1853-1872
Godel B, Barnes SJ, Maier WD (2007) Platinum-Group Elements in Sulphide Minerals, Platinum-Group Minerals, and Whole-Rocks of the Merensky Reef (Bushveld Complex, South Africa): Implications for the Formation of the Reef. Journal of Petrology 48(8):1569-1604 doi:10.1093/petrology/egm030
Godel B, Maier WD, Barnes S-J (2008) Platinum-Group Elements in the Merensky and J-M Reefs: A Review of Recent Studies. Journal of the Geological Society of India 72(5):595-609
Godel BM, Barnes SJ, Barnes S-J, Maier WD (2010) Platinum ore in 3D: Insights from high-resolution X-ray computed tomography. Geology 38:1127-1130
Godel BM, Barnes SJ, Gurer D, Austin P, Fiorentini ML (2012) Chromite in komatiites: 3D morphologies with implications for crystallization mechanisms. Contrib Mineral Petrol online, in press doi:10.1007/s00410-012-0804-y

Greenbaum D (1977) The chromitiferous rocks of the Troodos ophiolite complex, Cyprus. Economic Geology 72:1175-1194
Henderson P, Wood RJ (1981) Reaction relationships of chrome-spinels in igneous rocks - further evidence from the layered intrusions of Rhum and Mull, Inner Hebrides, Scotland. Contributions to Mineralogy and Petrology 78:225-229
Higgins MD (2000) Measurement of crystal size distribution. American Mineralogist 85:1105-1116
Hulbert LJ, Von Gruenewaldt G (1985) Textural and compositional features of chromite in the Lower and Critical Zones of the Bushveld Complex south of Potgietersrus. Economic Geology 80:872-895
Irvine TN (1975) Crystallization sequences in the Muskox intrusion and other layered intrusions—II. Origin of chromitite layers and similar deposits of other magmatic ores. Geochimica et cosmochimica acta 39(6-7):991-1020 doi:10.1016/0016-7037(75)90043-5
(1977) Origin of chromitite layers in the Muskox Intrusion and other stratiform intrusions: a new interpretation. Geology 5:273-277
Karato S-i, Dupas-Bruzek C, Rubie DC (1998) Plastic deformation of silicate spinel under the transition-zone conditions of the Earth's mantle. Nature 395(6699):266-269
Leblanc M (1980) Chromite growth, dissolution and deformation from a morphological view point: SEM investigations. Mineralium Deposita 15(2):201-210 doi:10.1007/bf00206514
Li C, Ripley EM, Sarkar A, Shin D, Maier WD (2005) Origin of phlogopite-orthopyroxene inclusions in chromites from the Merensky Reef of the Bushveld Complex, South Africa. Contributions to Mineralogy and Petrology 150(1):119-130 doi:10.1007/s00410-005-0013-z
Maier WD, Bowen MP (1996) The UG2-Merensky Reef interval of the Bushveld Complex northwest of Pretoria. Mineralium Deposita 31(5):386-393
Marsh BD (1988) Crystal size distribution (CSD) in rocks and the kinetics and dynamics of crystallization. Contributions to Mineralogy and Petrology 99:277-291
Mathez EA, Agrinier P, Hutchison R (1994) Hydrogen isotope composition of the Merensky Reef and related rocks, Atok section, Bushveld Complex. Economic Geology 89:791-802
McDonald JA (1965) Liquid immiscibility as one factor in chromite seam formation in the Bushveld Igneous Complex. Economic Geology 60:1674-1685
Naldrett A, Kinmaird J, Wilson A, Yudovskaya Ma, Chunnett G (2011a) Genesis of the PGE-Enriched Merensky Reef and Chromitite Seams of the Bushveld Complex. In: Ripley CLaEM (ed) Magmatic Ni-Cu AND PGE Deposits: Geology, Geochemistry, and Genesis, vol 17. Reviews in economic geology,
Naldrett AJ, Gasparrini E, Barnes SJ, Von Gruenewaldt G, Sharpe MR (1986) The Upper Critical Zone of the Bushveld Complex and the origin of Merensky-type ores. Economic Geology 81:1105-1117.
Naldrett AJ, Kinnaird J, Wilson A, Yudovskaya M, McQuade S, Chunnett G, Stanley C (2009a) Chromite composition and PGE content of Bushveld chromitites: Part 1 – the Lower and Middle Groups. Applied Earth Science : IMM Transactions section B 118(3):131-161 doi:10.1179/174327509x12550990458004
Naldrett AJ, Kinnaird JA, Wilson AH, Yudovskaya M, McQuade S, Chunnett G, Stanley C (2009b) Chromite composition and PGE content of Bushveld chromitites: Part 1 – the Lower and Middle Groups. App Earth Sci (Trans Inst Mining Metall Series B) 118:131-161 doi:10.1179/174327509X12550990458004
Naldrett AJ, Wilson A, Kinnaird J, Chunnett G (2009c) PGE Tenor and Metal Ratios within and below the Merensky Reef, Bushveld Complex: Implications for its Genesis. Journal of Petrology 50(4):625-659 doi:10.1093/petrology/egp015
Naldrett AJ, Wilson A, Kinnaird J, Yudovskaya M, Chunnett G (2011b) The origin of chromitites and related PGE mineralization in the Bushveld Complex: new mineralogical and

petrological constraints. Mineralium Deposita 47(3):209-232 doi:10.1007/s00126-011-0366-3
Nicholson DM, Mathez EA (1991) Petrogenesis of the Merensky Reef in the Rustenburg section of the Bushveld Complex. Contributions to Mineralogy and Petrology 107:293-309
Passchier CW, Trouw RAJ (2005) Microtectonics. Springer, Germany
Peters T, Kramers JD (1974) Chromite deposits in the ophiolite complex of northern Oman. Mineralium Deposita 9:253-259
Prior DJ, Boyle AP, Brenker F, Cheadle MC, Day A, Lopez G, Peruzzi L, Potts G, Reddy S, Spiess R, Timms NE, Trimby P, Wheeler J, Zetterstrom L (1999) The application of electron backscatter diffraction and orientation contrast imaging in the SEM to textural problems in rocks. American Mineralogist 84(11-12):1741-1759
Reddy SM, Timms NE, Pantleon W, Trimby P (2007) Quantitative characterization of plastic deformation of zircon and geological implications. Contributions to Mineralogy and Petrology 153(6):625-645 doi:10.1007/s00410-006-0174-4
Ricard LP, Godel BM, Chanu J-B (2012) CSDToolbox 1.0: A MATLAB program for the analysis of crystal-size distribution of large datasets. Computers & Geosciences (0) doi:10.1016/j.cageo.2012.01.010
Roeder PL, Campbell IH (1985) The effect of postcumulus reactions on compositions of chrome-spinels from the Jimberlana Intrusion. Journal of Petrology 26:763-786
Shore M, Fowler AD (1999) The origin of spinifex texture in komatiites. Nature 397:691-694
Spandler C, Mavrogenes J, Arculus R (2005) Origin of chromitites in layered intrusions: Evidence from chromite-hosted melt inclusions from the Stillwater Complex. Geology 33(11):893 doi:10.1130/g21912.1
Talkington RW, Watkinson DH, Whittaker PJ, Jones PC (1983) Platinum-group minerals and other solid inclusions in chromite of ophiolitic complexes: Occurrence and petrological significance. TMPM Tschermaks Mineralogische und Petrographische Mitteilungen 32(4):285-301 doi:10.1007/bf01081619
Wheeler, Wheeler J, Prior, Prior D, Jiang, Jiang Z, Spiess, Spiess R, Trimby, Trimby P (2001) The petrological significance of misorientations between grains. Contributions to Mineralogy and Petrology 141(1):109-124
Wheeler J, Jiang Z, Prior DJ, Tullis J, Drury MR, Trimby PW (2003) From geometry to dynamics of microstructure: using boundary lengths to quantify boundary misorientations and anisotropy. Tectonophysics 376(1-2):19-35 doi:10.1016/j.tecto.2003.08.007
Zhou M-F, Kerrich R (1992) Morphology and composition of chromite in komatiites from the Belingwe Greenstone Belt, Zimbabwe. Canadian Mineralogist 30:303-317

Table and figure captions

Table 1 Average compositions of the chromite crystals from the lower (LC) and upper (UC) chromitite layer from the Merensky Reef. Oxide values are in wt %.

Figure 1 a) Simplified geological map of the western limb of the Bushveld complex (modified after Von Gruenewaldt et al., (1986, 1989). b) Simplified stratigraphy of the Bushveld Complex according to Eales and Cawthorn (1996) c) Sketch of the Merensky Reef slab from which the samples were drilled that comprise whole Merensky Reef stratigraphy.

Figure 2 Photomicrographs of the Merensky Reef thin sections showing microstructures a) Contact between coarse-grained melanorite, lower chromitite and footwall anorthosite. Yellow line indicates amoeboidal chromite crystal shape. Red line indicates idiomorphic chromite crystal shape. b) Large *amoeboidal* chromite crystal from the lower chromitite layer. c) Deformation twins in plagioclase (Plg) in coarse grained melanorite. d) Contact between melanorite and upper chromitite layer. e) Fine-grained idiomorphic chromite crystals from the upper chromitite layer. f) Plagioclase (Plg) oikocryst showing deformation twins, enclosing idiomorphic chromite crystals. a, b, e, f: plane polarised transmitted light; c,d: reflected light.

Figure 3 a) An image of 3D volume obtained by high-resolution X-ray computed tomography of chromite crystals from lower chromitite layer (light grey). Set of four slices is showing change in the morphology of the grain within the sample. Light blue grains are chromite crystals; dark blue background represents silicate minerals. b) An image of 3D chromite grain from the lower chromitite layer, containing over fifty individual silicate inclusions (red). c) An image of 3D volume obtained by high-resolution X-ray computed tomography of idiomorphic chromite crystals from the upper chromitite layer.

Figure 4 a) Binary image of a thin section from the lower chromitite layer used for the image analysis. b) Crystal-size distribution curve of the lower chromitite layer using equivalent circle diameter (ECD) as a size parameter. c) Binary image of a thin section from the upper chromitite layer used for the image analysis. d) Crystal-size distribution curve (blue) of the upper chromitite layer. Dotted red line represents regression curve with the slope of -0.012 and intercept of 1.203.

Figure 5 a) EBSD map of a sample from lower chromitite layer. Step size of the map is 20μm. Inverse pole figure map is superimposed on band contrast map. Band contrast map represents the quality of the electron backscatter (EBS) patterns where as Inverse pole figure

map shows the orientation of each crystal plane relative to the X direction of the sample reference frame. Full red, green and blue colour are assign to the grains whose <100>, <110> or <111> axes are parallel to the projection of the inverse pole figure. Intermediate orientations are coloured by an RGB mixture of the primary axes. b) Grain size map for the lower chromitite layer defined by circle equivalent diameter. c) Folded inverse pole figures of the chromite crystals are plotted as one point per grain on equal-area projection of the lower hemisphere. Number of points: 82. The colour of the grains is corresponding to grain size map b). d) Misorientation angle distribution of uncorrelated data for the lower chromitite layer.

Figure 6 EBSD map of a sample from upper chromitite sample. Step size of the map is 15 μm. Inverse pole figure map is superimposed on band contrast map. b) Grain size map for the upper chromitite defined by circle equivalent diameter. c) Folded inverse pole figures of the chromite crystals data are plotted as one point per grain on equal-area lower hemisphere projection. Number of points: 321. The colour of the grains is corresponding to grain size map b). d) Misorientation angle distribution of uncorrelated data for the upper chromitite layer.

Figure 7 a) EBSD maps showing lattice distortion within chromite crystals (grains 1 to 3). Cumulative misorientation map for amoeboid chromite crystals from the lower chromitite layer. Colours indicate contours on misorientation angle relative to lattice orientation at the (arbitrary) position marked by a red cross. Maximum misorientation angle for grains 1 to 3 is 10°. b) Crystallographic orientation data for the grains 1 to 3 corresponding to the pole figures PF1 – PF3. Data is presented on lower hemisphere equal area pole figure. Three axes, (001), (110) and (111) are presented on a single pole figure plot. c) EBSD maps showing lattice distortion within chromite crystals (grains 4 to 6). Maximum misorientation angle for grains for grains 4 to 6 is 5°. The red lines represent subgrain boundaries larger than 1°.

Grains from 1 to 3 are large amoeboidal crystals where as grains from 4 to 6 are characterized with idiomorphic shape.

Figure 8 a) Cumulative misorientation map showing maximum misorientation of 3° for the individual idiomorphic grains from upper chromitite layer. Grains 1 and 2 show areas with apparent 2° misorientation; these areas are artefacts due to broad ion beam polishing. b) Inverse pole figure map parallel to the X direction of the sample reference frame for the cluster of six different idiomorphic grains. Black lines are >20° grain boundaries. c) Misorientation axes in the sample coordinate system plots for 6 different profiles across boundaries between the 6 idiomorphic grains.

Figure 9 Compositional variations for the chromite grains from both lower and upper chromitite layer. Comparative data from Li, et al. (2005) and Godel, et al. (2008). Values from Li, et al. (2005) are averaged values.

Figure 10 a) Backscatter image of an amoeboidal chromite crystal from the lower chromitite layer. b) Fe element map. c) Ti element map showing needle like (yellow rectangular -d) and more globular rutile (red rectangular - e) exsolutions.

Figure 11 a) Backscatter image of the idiomorphic chromite from the upper chromitite layer. b) Fe element map. c) Ti element map showing globular and interstitial rutile phase, and needle like (white rectangular - d) rutile exsolutions.

Figure 12 Mean misorientation versus area versus solidity bubble plots of a) lower chromitite layer; and b) upper chromitite layer. Size of the bubble is a function of solidity values with smallest bubble corresponding to the lowest solidity values. Gray area on a and b) represents the field of upper chromitite layer data superimposed on the lower chromitite layer data and lower chromitite layer data superimposed on the upper chromitite layer data.

Figure 13 Models for the formation of the inclusion bearing chromite crystals. a) Schematic representation of the sintering process of crystals that have different crystallographic

orientation. Simplified pole figure plot shows poles to [100] lattice planes of each of the sintered crystals falls in a different area of the stereographic projection. b) Schematic representation of the sintering process followed by recrystallisation to a single crystal. New grain plots on the stereographic projection as a single crystal with mild distortion due to the later deformation that caused formation of subgrain boundaries. c) Chromites crystallizing as single-crystal dendrites and subsequently undergoing partial recrystallisation with trapping of silicate inclusions. Such re-modified dendritic crystals would plot as single crystals on the stereographic projection. Deformation of these grains would give rise to dispersion of lattice plan orientations as in (b).

Figure 14 Crystallisation and compaction model for the Merensky Reef. a) First stage shows the crystallisation of the lower chromitite layer and coarse-grained melanorite. b) Input of a new magma responsible for the formation of the upper chromitite layer and modification of dendrites (b_1). c) Cooling of the magmatic column results in mobilisation of intercumulus melt and formation of compaction-related deformation. Deformation is selectively recorded according to the shape and size of the chromite crystals (c_1 and c_2). Red lines in amoeboidal chromites schematically represent subgrain boundaries.

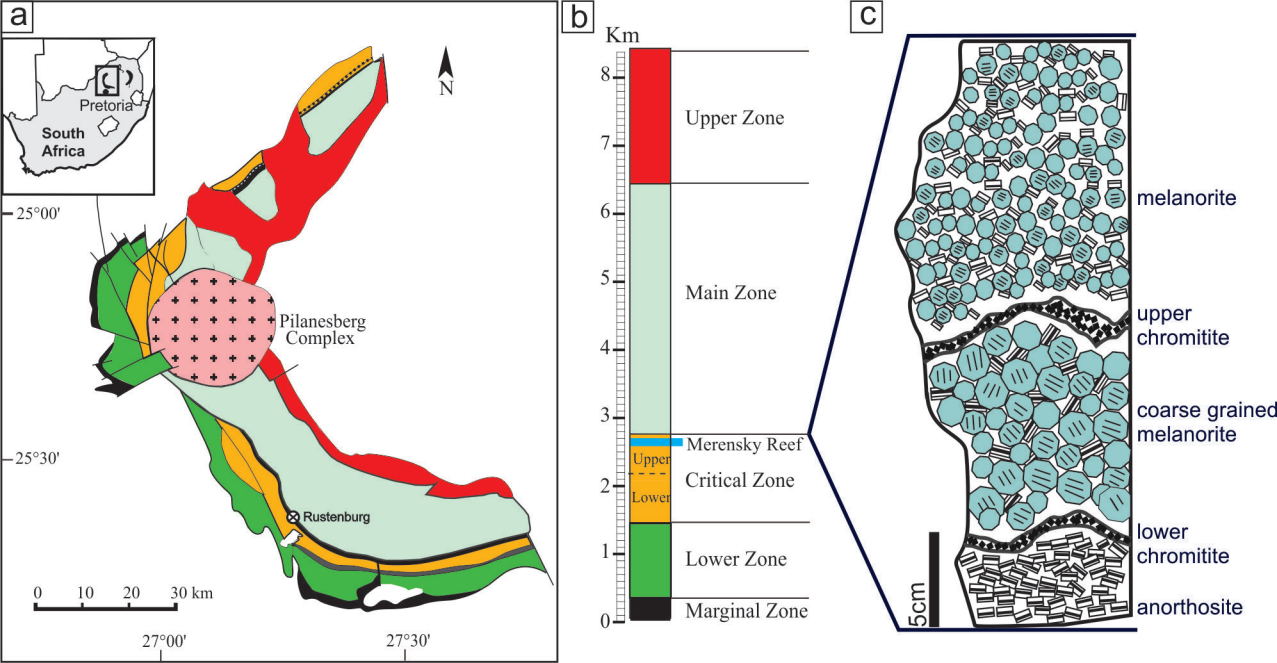
a
Pretoria
South Africa
N
25°00'
25°30'
Pilanesberg Complex
Rustenburg
0 10 20 30 km
27°00'
27°30'
b
Km
8
7
6
5
4
3
2
1
0
Upper Zone
Main Zone
Merensky Reef
Upper
Lower
Critical Zone
Lower Zone
Marginal Zone
c
melanorite
upper chromitite
coarse grained melanorite
lower chromitite
anorthosite
5cm

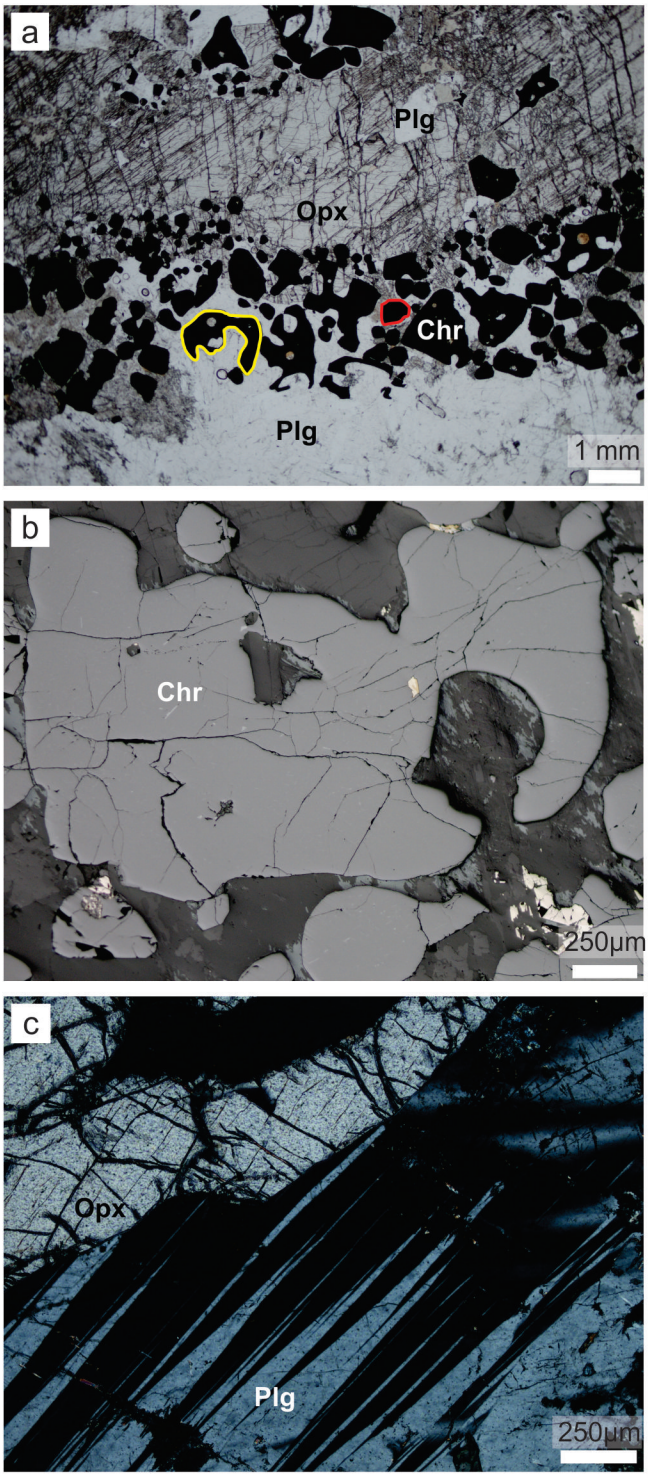

Lower Chromitite photomicrographs

Upper Chromitite photomicrographs

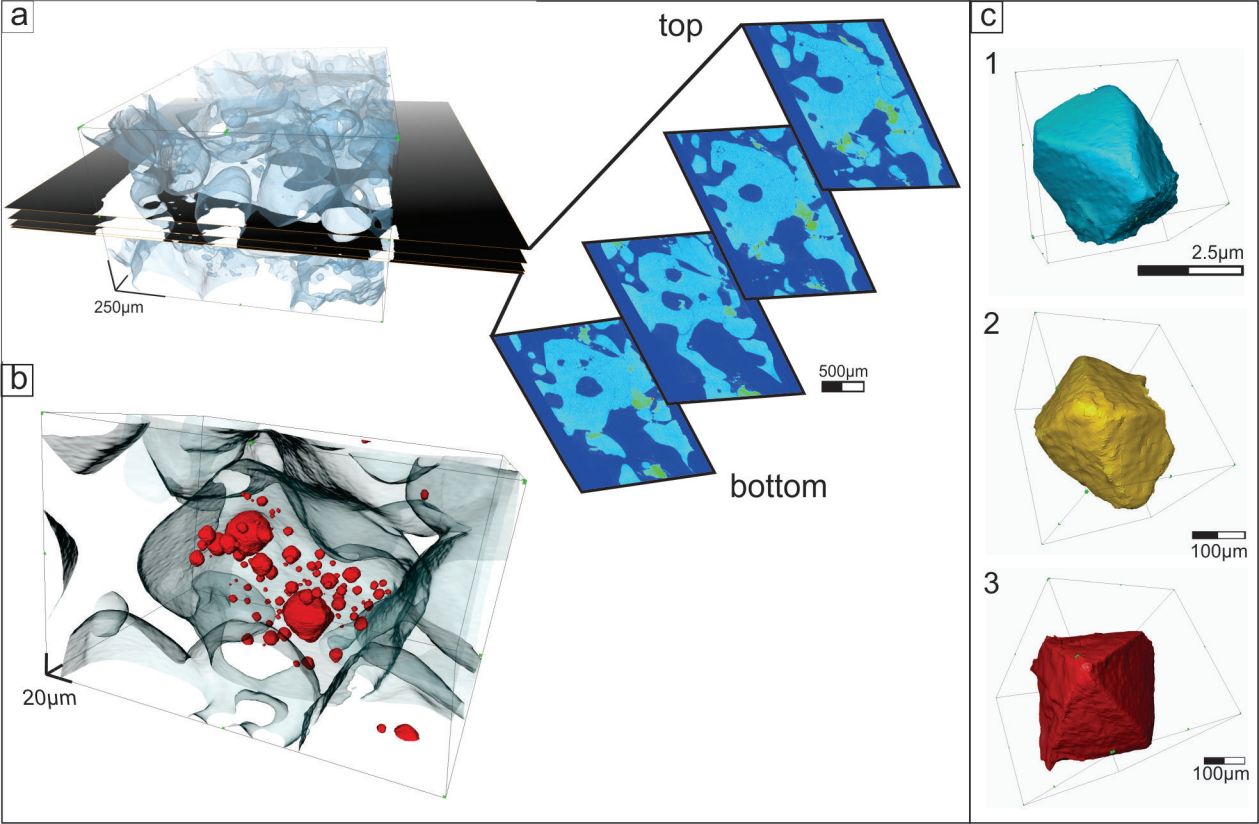
a
top
250µm
500µm
bottom
b
20µm
c
1
2.5µm
2
100µm
3
100µm

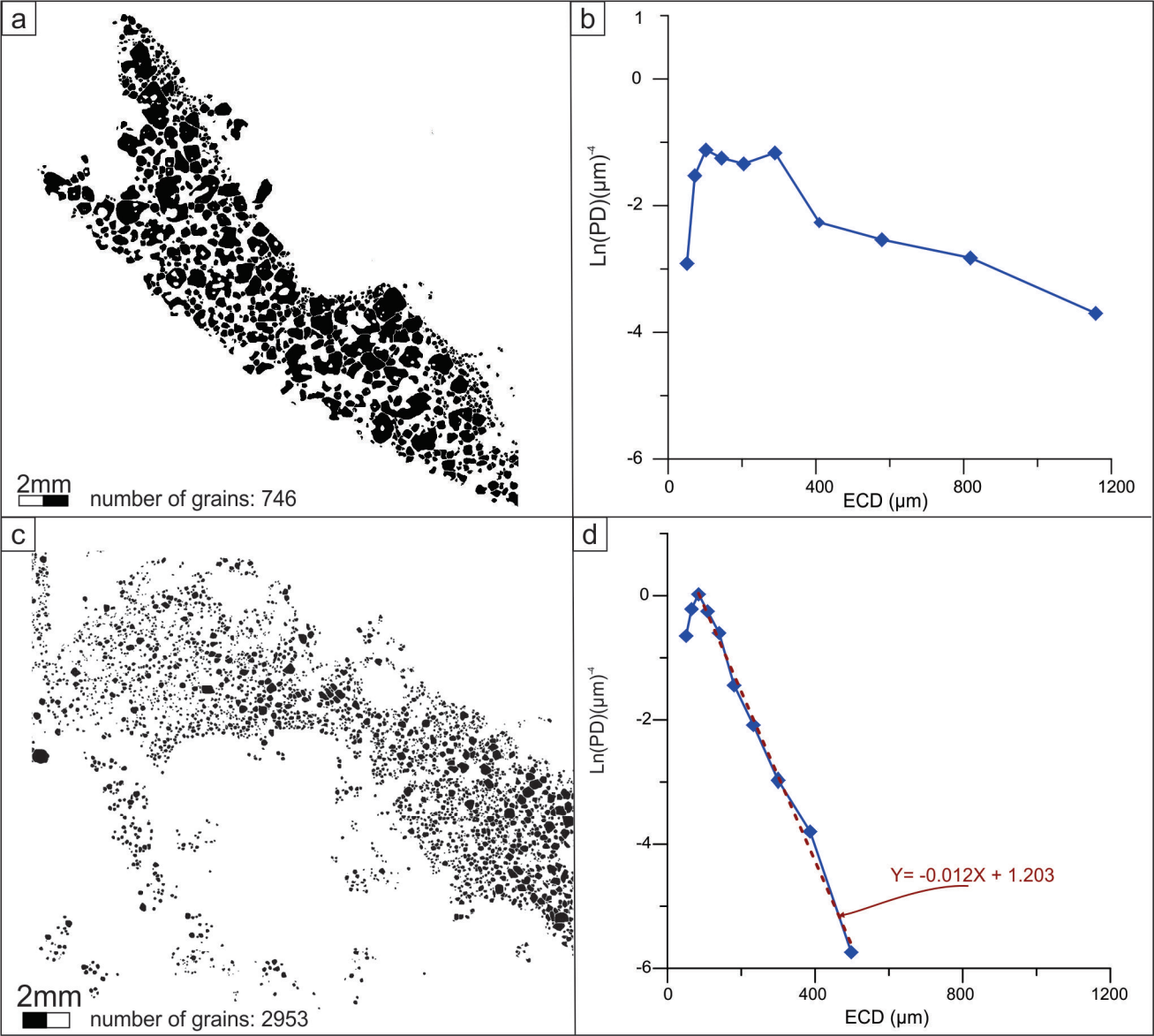
a
2mm
number of grains: 746
b
1
0
-2
-4
-6
Ln(PD)(μm)-4
0
400
800
1200
ECD (μm)
c
2mm
number of grains: 2953
d
0
-2
-4
-6
Ln(PD)(μm)-4
Y= -0.012X + 1.203
0
400
800
1200
ECD (μm)

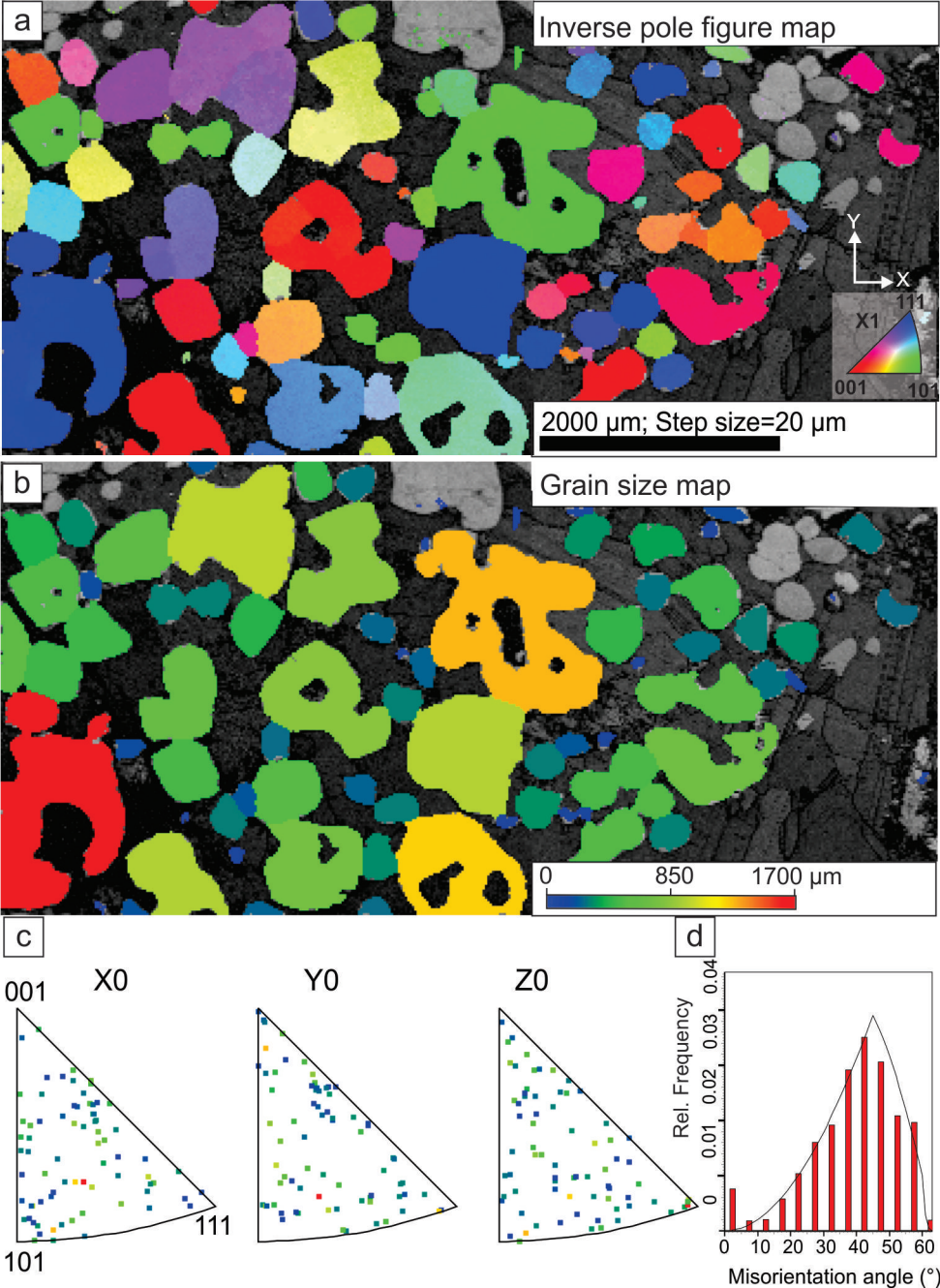
a
Inverse pole figure map
Y
X
111
X1
001
101
2000 µm; Step size=20 µm
b
Grain size map
0
850
1700 µm
c
001
X0
Y0
Z0
111
101
d
Rel. Frequency
0
0.01
0.02
0.03
0.04
0
10
20
30
40
50
60
Misorientation angle (°)

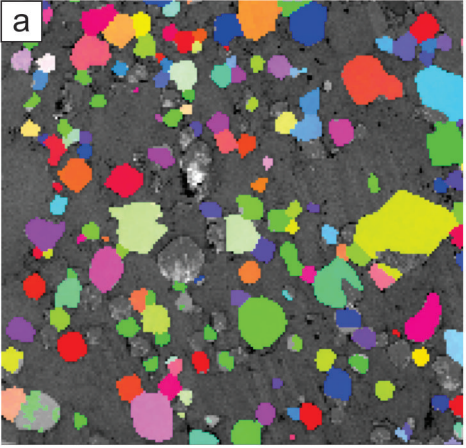

Inverse pole figure map

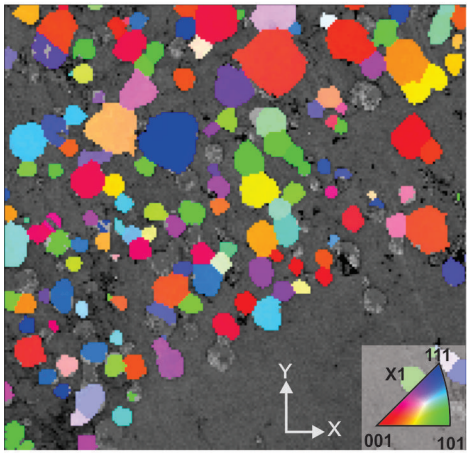

2000 μm; Step size 15μm

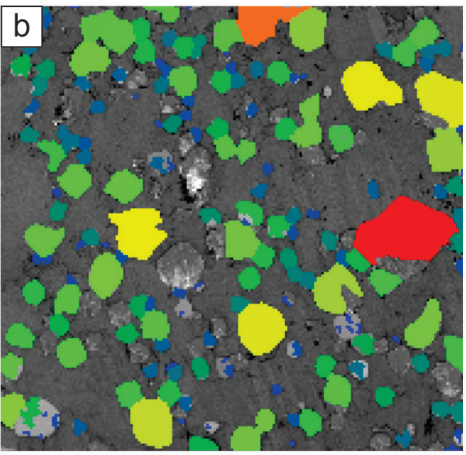

Grain size map

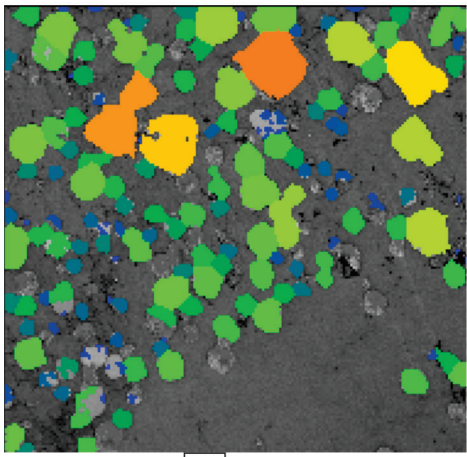

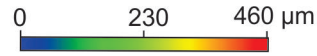

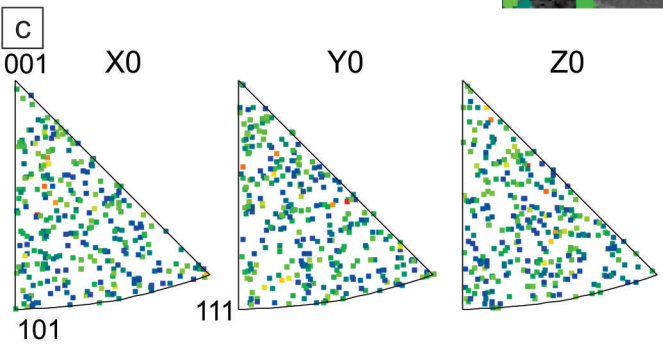

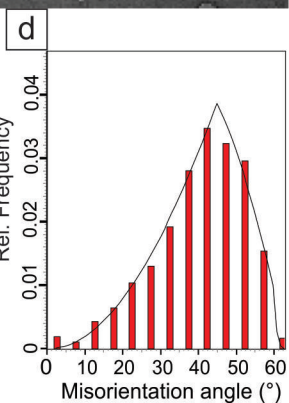

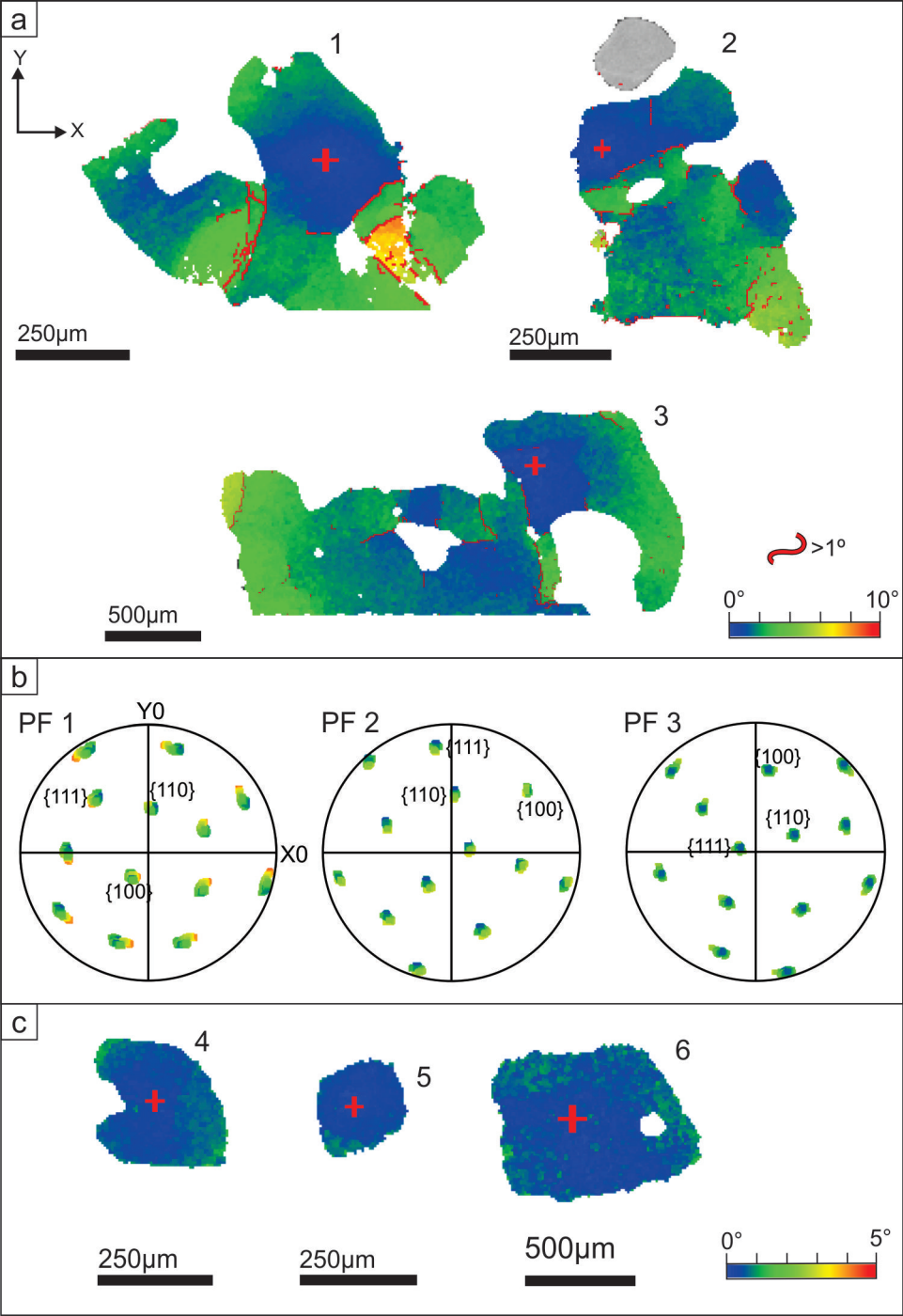
a
Y
X
1
250µm
2
250µm
3
500µm
>1°
0°
10°
b
PF 1
Y0
X0
{111}
{110}
{100}
PF 2
{111}
{110}
{100}
PF 3
{100}
{110}
{111}
c
4
250µm
5
250µm
6
500µm
0°
5°

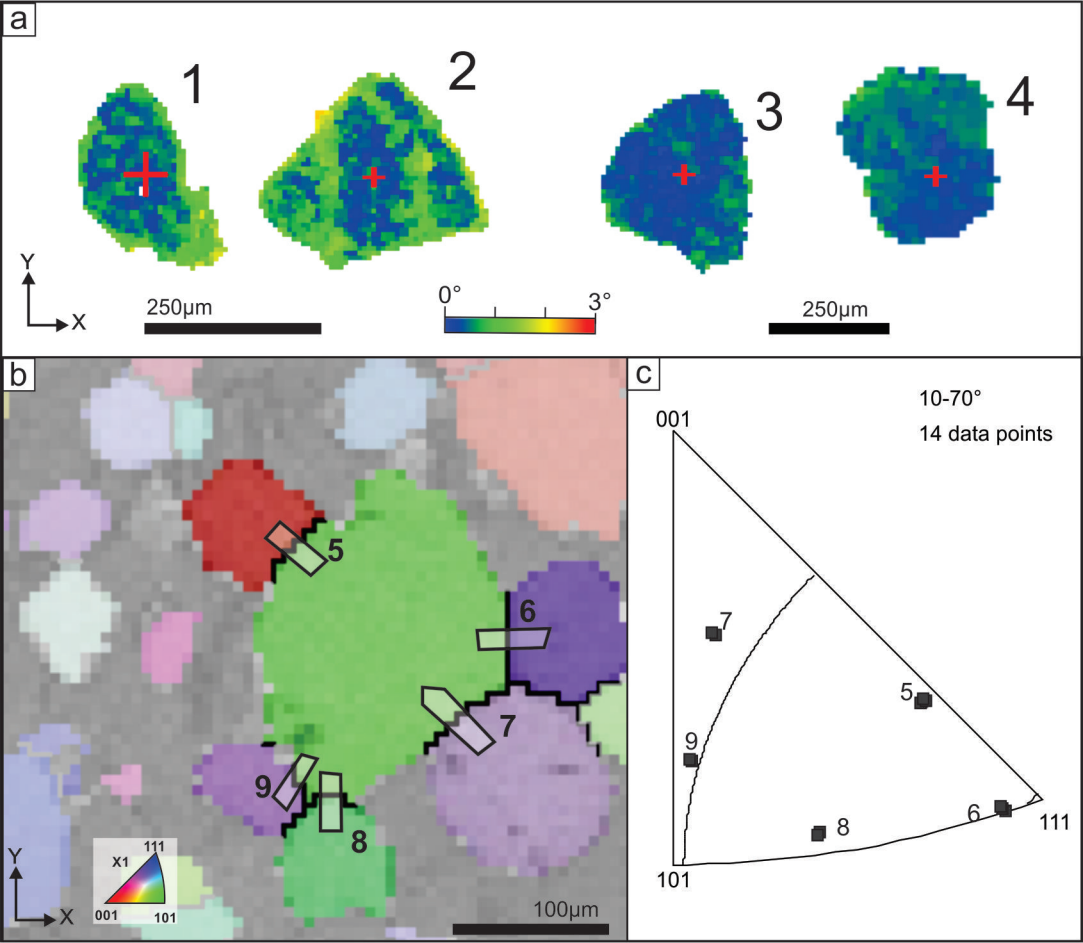
a
1
2
3
4
Y
X
250µm
0°
3°
250µm
b
5
6
7
9
8
Y
X
X1
111
001
101
100µm
c
10-70°
14 data points
001
111
101
7
5
9
8
6

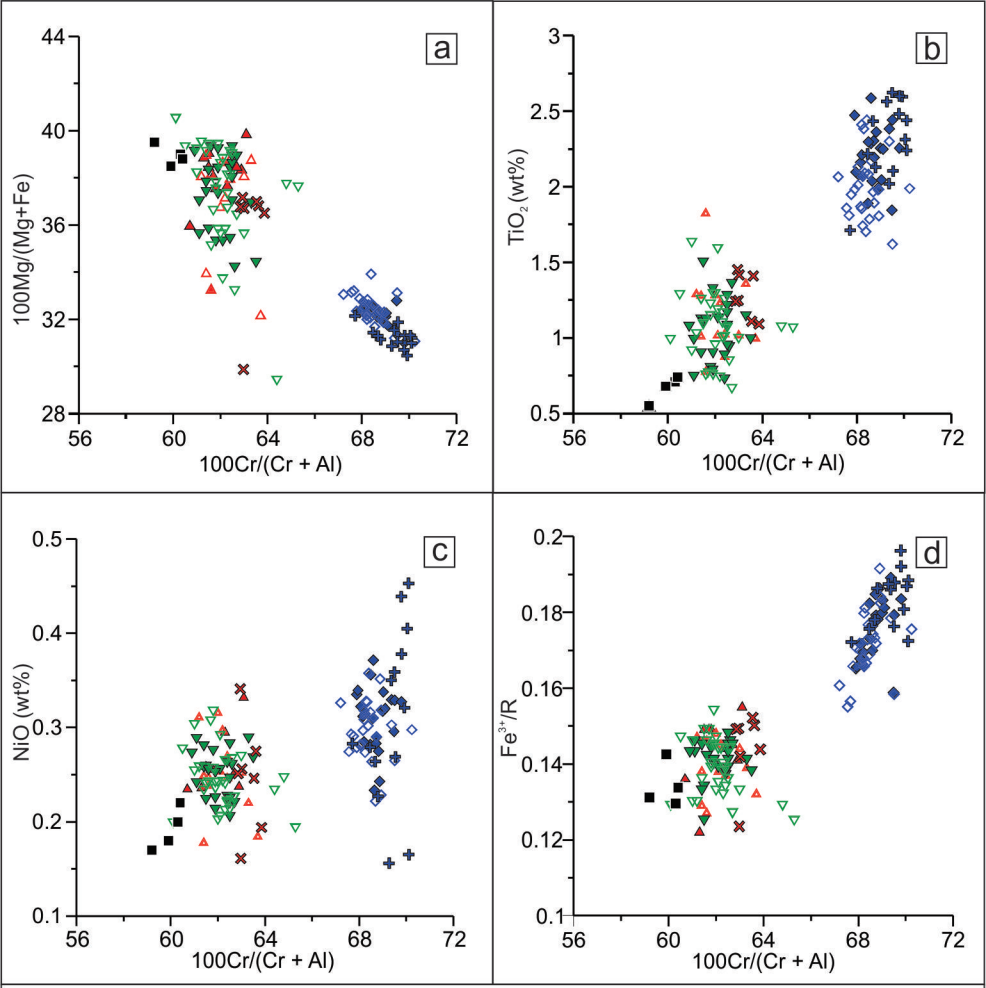
a
100Mg/(Mg+Fe)
100Cr/(Cr + Al)
b
TiO2 (wt%)
100Cr/(Cr + Al)
c
NiO (wt%)
100Cr/(Cr + Al)
d
Fe3+/R
100Cr/(Cr + Al)
this study
UC core
UC rim
LC Idiomorphic core
LC Idomorphic rim
LC Ameobodial core
LC Ameoboidal rim
Godel et al 2008
LC
UC
Li et al 2005
LC

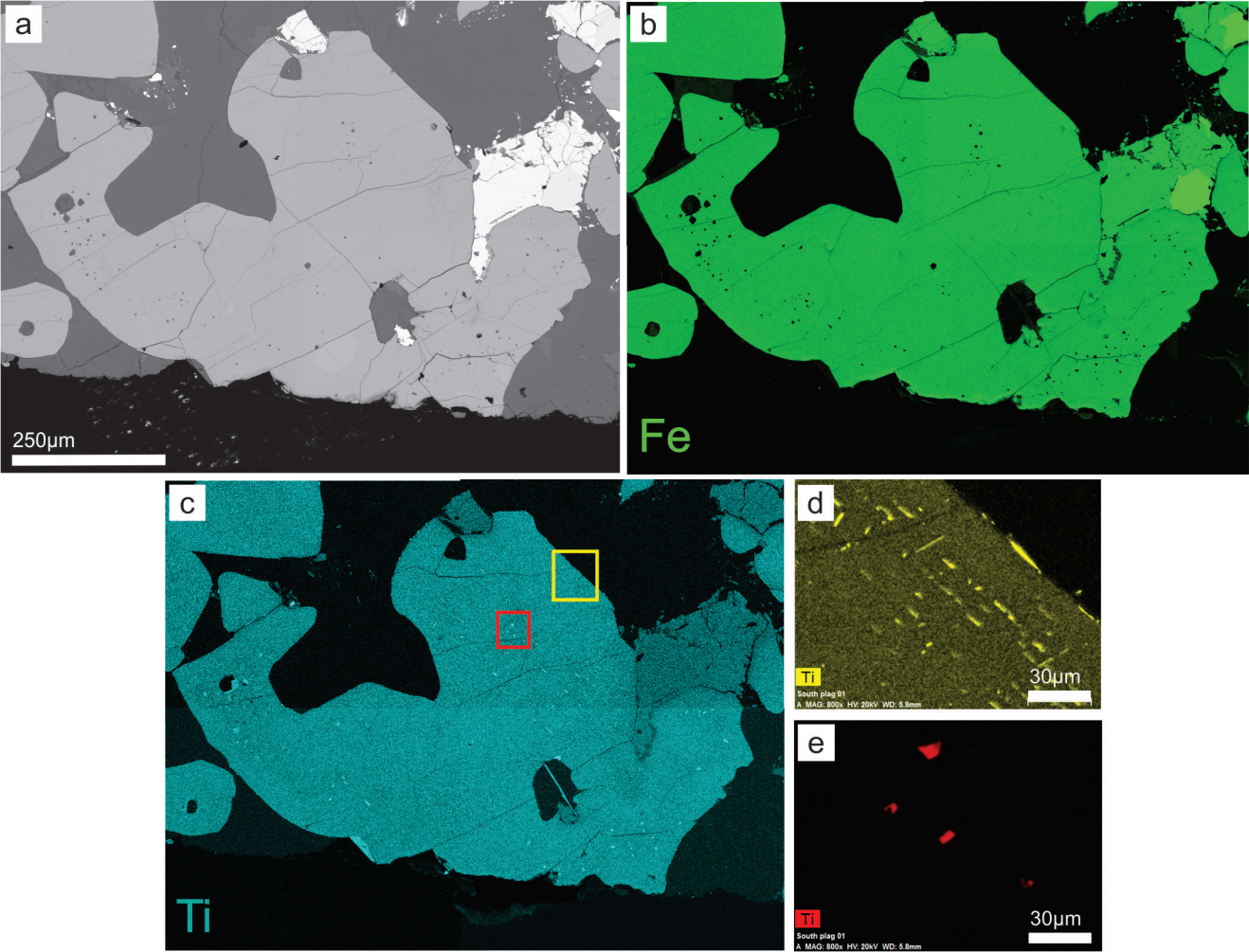
a
250μm
b
Fe
c
Ti
d
Ti
30μm
South plag 01
A MAG: 800x HV: 20kV WD: 8.8mm
e
Ti
30μm
South plag 01
A MAG: 800x HV: 20kV WD: 8.8mm

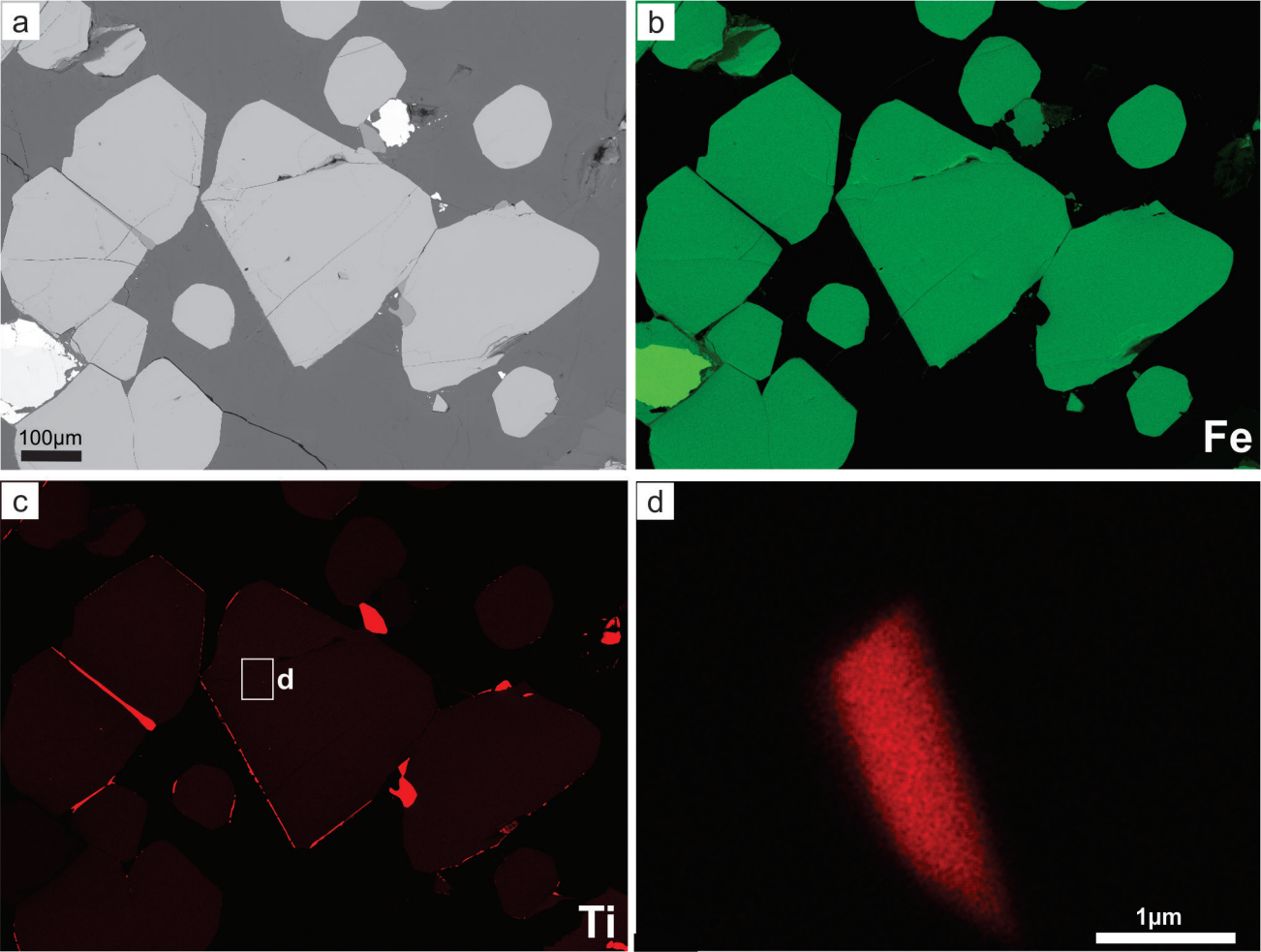
a
100μm
b
Fe
c
d
Ti
d
1μm

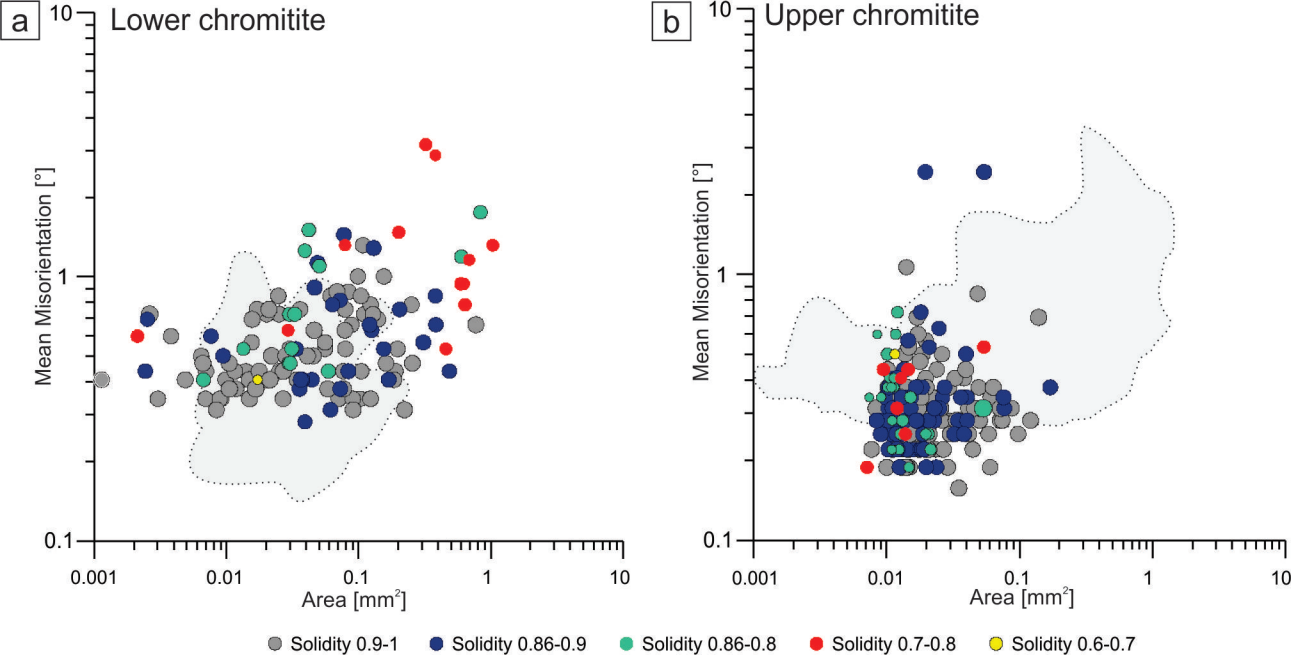
a
Lower chromitite
b
Upper chromitite
Mean Misorientation [°]
10
1
0.1
0.001
0.01
0.1
1
10
Area [mm²]
Solidity 0.9-1
Solidity 0.86-0.9
Solidity 0.86-0.8
Solidity 0.7-0.8
Solidity 0.6-0.7

Origin of amoebidal chromites

a

Sintering

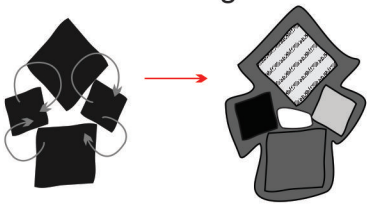

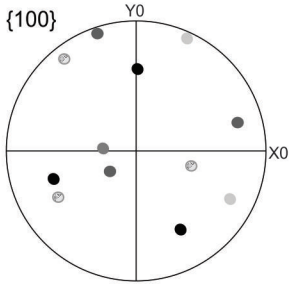

b

Sintering followed by recrystallization

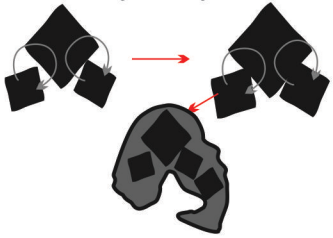

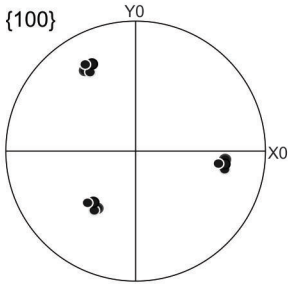

c

Recrystallisation of dendritic chromites

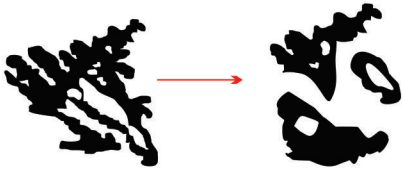

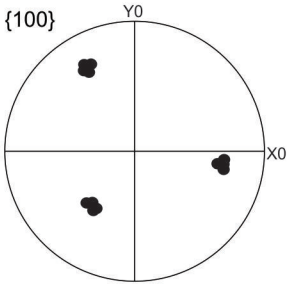

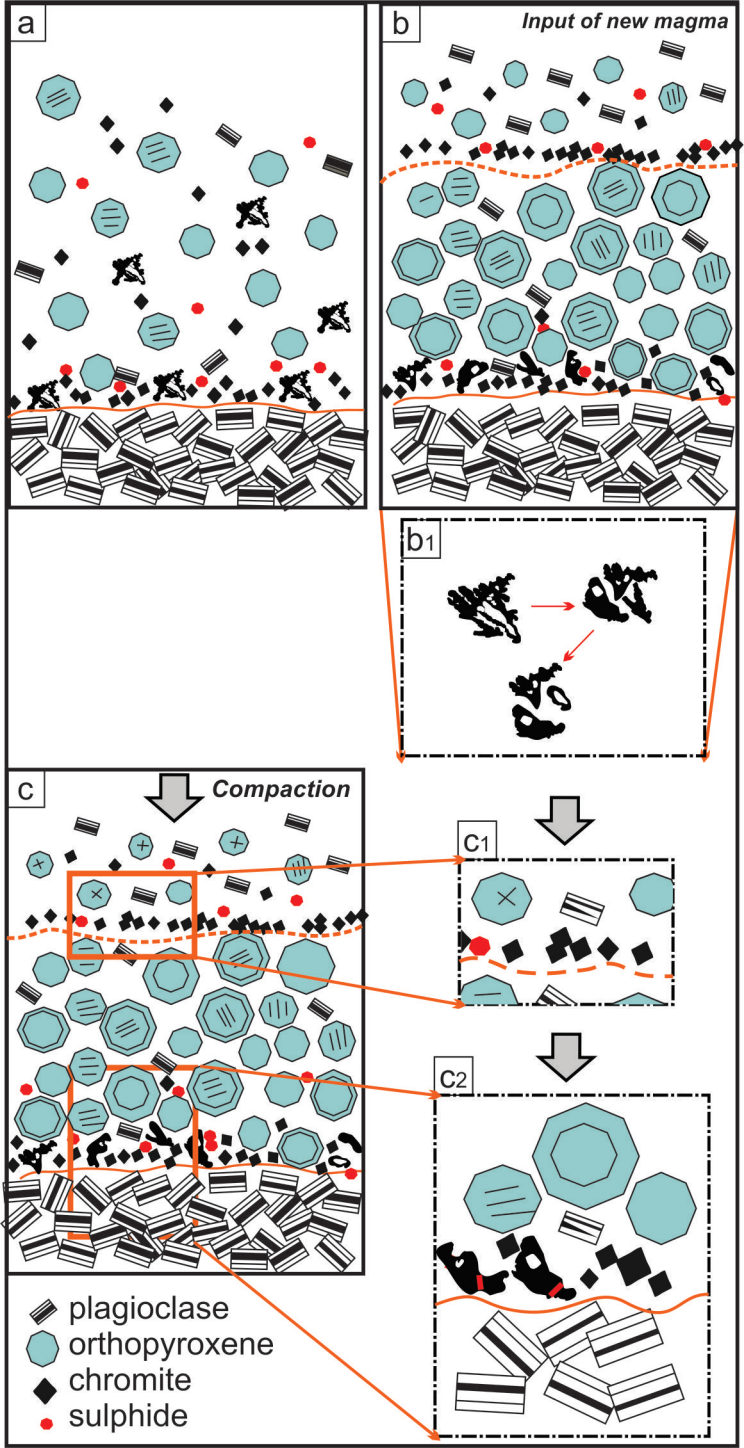
a
b
Input of new magma
b1
c
Compaction
c1
c2
plagioclase
orthopyroxene
chromite
sulphide